Fast assembly and *in vivo* coalescence of ParB biocondensates involved in bacterial DNA partition

Perrine Revoil[1], Linda Delimi[2], Jérôme Rech[1], Josh Cailhau[2], François Cornet[1], Jean-Charles Walter[2]* and Jean-Yves Bouet[1]*

[1] Laboratoire de Microbiologie et Génétique Moléculaires, Centre de Biologie Intégrative (CBI), Centre National de la Recherche Scientifique (CNRS), Université de Toulouse, F-31062 Toulouse, France.

[2] Laboratoire Charles Coulomb (L2C), CNRS, Université de Montpellier, Montpellier, France.

*Correspondence should be addressed to jean-yves.bouet@univ-tlse3.fr and jean-charles.walter@umontpellier.fr

Classification: Biological science

Keywords: Biomolecular condensates, Condensate coalescence, ParABS system, Partition complex, ParB, DNA segregation.

Abstract

Faithful DNA segregation in bacteria relies on ParABS systems, in which ParB assembles into condensates at centromere-like *parS* sites and ParA, an ATPase, spatially organizes these complexes. Yet how ParB condensates preserve their dynamic behavior without collapsing into a single droplet has remained unclear. Here, we combined inducible chromosome degradation with quantitative imaging to dissect the kinetics and physical principles governing ParB condensate dynamics *in vivo*. In the absence of the nucleoid, ParB condensates diffuse freely and coalesce within seconds upon encounter, following Brownian first-encounter statistics. Strikingly, condensates operate near the fusion-separation boundary, such that minimal energy is sufficient to split droplets after replication, thereby preventing irreversible coalescence. Using different mutants, we further show that proper condensate assembly is essential for coalescence. These findings uncover a dual role of ParA: beyond tethering condensates to the nucleoid to limit mobility and prevent uncontrolled fusion, ParA also promotes a ParB state competent for condensate assembly and thus coalescence, likely by enhancing ParB-ParB interactions. Finally, condensates rapidly disassemble and reassemble upon 1,6-hexanediol treatment, underscoring their reversible, dynamic nature and the stabilizing contribution of ParB-DNA interactions. Together, our results establish ParB partition complexes as *bona fide* biocondensates and reveal how their dynamics are finely tuned by ParA to ensure robust and faithful DNA segregation. More broadly, these findings highlight regulated phase separation as a key organizing principle of bacterial replicons.

Significance statement

Faithful chromosome and plasmid segregation is essential for bacterial survival, yet the underlying physical principles remain unclear. We show that ParB partition complexes are *bona fide* biomolecular condensates whose fusion–fission dynamics are tightly regulated to prevent collapse into a single droplet. Using quantitative imaging with inducible chromosome degradation, we demonstrate that ParB condensates operate near the fusion-separation boundary, where minimal energy allows splitting. We further uncover a dual role of the ATPase ParA: tethering condensates to the nucleoid and promoting their assembly. These findings establish partition complexes as phase-separated organelles and reveal how their dynamics are tuned to ensure robust DNA segregation, underscoring phase separation as a key principle of bacterial cell organization.

Introduction

Bio-molecular condensates, also known as membrane-less organelles, are key players in living organisms, facilitating diverse biological processes important for cell function (Alberti et al., 2025; Boeynaems et al., 2018). They have been widely reported in eukaryotes, and more recently in bacteria where they concentrate proteins and nucleic acids without the use of a lipid membrane (Azaldegui et al., 2021; Cohan and Pappu, 2020). In bacteria, these bio-condensates are involved in processes, such as transcription (Ladouceur et al., 2020), mRNA decay (Al-Husini et al., 2018), and the partitioning of diverse cargos, *e.g.*, carboxysomes in autotrophic bacteria (Basalla et al., 2023; MacCready et al., 2020) and DNA centromeres from plasmids and chromosomes (Guilhas et al., 2020).

The major driver of active DNA partitioning in bacteria is the ParABS system, present in most low-copy-number plasmids and the only one present on chromosomes (Bouet and Funnell, 2019). The ParABS system is composed of three components: two proteins, ParA and ParB, and a centromeric sequence, *parS*. Together, these elements are both necessary and sufficient to ensure accurate plasmid transmission. ParB assembles into a large nucleoprotein complex at *parS*. ParA ATPases are involved in the positioning and partitioning of a variety of cargos by simply interacting, in its nucleoid-bound form, with a component of the cargo (Lutkenhaus, 2012). The interactions of ParA with the cargo's partner stimulates its ATPase activity and its release from DNA (Ah-Seng et al., 2009; MacCready et al., 2018; Vecchiarelli et al., 2010), driving the cargo-dependent depletion of ParA locally on the nucleoid and promoting directed motion of the cargo towards increased concentrations of ParA (Hu et al., 2021; Hu et al., 2015; Hwang et al., 2013; Walter et al., 2017). In the case of the ParABS system, a subset of ParA is also found associated with high-density-regions of the nucleoid and is involved in anchoring ParB condensates within the nucleoid (Hu et al., 2021; Le Gall et al., 2016). Following DNA replication and duplication of this complex, ParA mediates the separation and intracellular relocation of these complexes to quarter-cells positions ensuring their distribution in daughter cells upon cell division (Bouet and Funnell, 2019).

Partition complexes regroup over 90% of ParB at centromere sites (Sanchez et al., 2015). Their assembly are initiated by a sequential multi-step process (Walter et al., 2020): (i) specific binding of ParB to *parS*, usually a 16-bp DNA motif (Lin and Grossman, 1998; Livny et al., 2007; Pillet et al., 2011), (ii) binding of CTP to *parS*-bound ParB (Osorio-Valeriano et al., 2019; Soh et al., 2019), (iii) conversion of ParB into a clamp inducing its release from *parS* (Soh et al., 2019), (iv) diffusion at short distances over *parS*-proximal DNA (Alaoui et al., 2025; Soh et al., 2019), and lastly (v) clamp opening followed by ParB unloading. ParB thus cycles between open and clamped forms, called the ParB-CTP cycle, enabling the loading of ~10 ParB

clamps from *parS* sites (Delimi et al., 2025; Walter et al., 2020). Notably, partition complexes exhibit properties characteristic of biomolecular condensates (Babl et al., 2022; Guilhas et al., 2020), with a difference in ParB density between the condensed and dilute phases likely through phase separation (Azaldegui et al., 2021; Monterroso et al., 2024). This latter property is proposed to account for the strong local enrichment of ParB in condensates. This recruitment involves the activation of a CTP-dependent molecular switch that enhances ParB-ParB interactions (Delimi et al., 2025).

Biomolecular condensates exhibit several hallmark properties of liquid-like objects, such as spherical shapes, rapid exchange of components between condensed and diffuse phases, and coalescence into single droplets (Shin and Brangwynne, 2017). Partition complexes displays these features *in vivo*, including rapid exchange of ParB between complexes (Debaugny et al., 2018; Osorio-Valeriano et al., 2021), slower intracellular mobility of ParB inside rounded condensates compared to outside (~100-fold reduction) (Guilhas et al., 2020), and the fusion of ParB condensates when ParA is degraded (Guilhas et al., 2020). At thermodynamic equilibrium, in a finite and confined system, phase separation with a condensed phase minimizes interfacial free energy by forming a single spherical droplet within a dilute continuous phase. Relaxation toward the lowest-energy state is typically achieved through droplet coalescence or Ostwald ripening (Hyman et al., 2014). In ParABS systems, however, this passive tendency toward coalescence conflicts with the functional requirement to maintain multiple, *parS*-nucleated ParB condensates in distinct positions to ensure faithful DNA partition. Previous work showed that impairing ParA activity, via an inducible degron system, allowed ParB condensates to undergo fusion events (Guilhas et al., 2020). However, these events occurred slowly, presumably due to continuous high expression of ParA before its progressive degradation, thus hindering further investigation of this important feature.

Here, we developed an inducible chromosome degradation system to dissect the behavior of ParB condensates in the absence of the nucleoid. In this context, ParB condensates diffuse freely and coalesce within seconds upon encounter, providing a system suitable for kinetic measurements. We further show that condensate assembly is rapid, reversible, and dependent on hydrophobic interactions, as revealed by hexanediol sensitivity. Importantly, these analyses uncover a previously unappreciated role of ParA, beyond nucleoid tethering, in promoting ParB condensate assembly. Together, these functions regulate the fusion-fission balance of ParB condensates, maintaining their dynamic stability and ensuring robust, faithful segregation of bacterial DNA.

Results

Chromosome depletion triggers coalescence of ParB condensates

ParB condensates are typically anchored within the nucleoid via interactions with ParA, which binds to the high-density regions of DNA (Le Gall et al., 2016). To investigate the dynamics and conditions that promote fusion of ParB condensates, we developed a strategy to disrupt this anchoring by selectively removing the bacterial chromosome. We hypothesized that depleting the nucleoid would free ParB condensates to diffuse throughout the cytoplasm, facilitating their coalescence, if any. To test this, we employed a method for specific and progressive chromosome degradation while preserving plasmid integrity (Stracy et al., 2021). We constructed an *E. coli recA* strain (DLT4151) carrying four I-SceI restriction sites evenly distributed across the chromosome (Fig. 1A). This strain was transformed with pSN01, which expresses the I-SceI endonuclease under the control of arabinose, enabling inducible double-strand breaks and subsequent chromosome degradation. The amount of nucleoid per cell was monitored over time using DAPI staining and fluorescence microscopy (Fig. 1B, left panels). Upon arabinose-induced I-SceI production, DAPI fluorescence intensity gradually decreased to near-baseline levels over ~100 minutes, confirming progressive loss of chromosomal DNA (Supplementary Fig. S1A-C). By 120 minutes post-induction (T120), chromosomal DNA was extensively degraded in nearly all cells.

We then examined the behavior of ParB condensates in the absence of the nucleoid. F plasmids producing ParB-mVenus fusion proteins were introduced in the DLT4151 strain, which was further transformed with pSN01. In steady-state growth, prior to induction (T0), cells carrying the 100-kbp F plasmid (F1-10B04) typically exhibited two ParB-mVenus foci. After chromosome degradation (T120), 88.4% of cells contained only a single focus (Fig. 1B, right panel and Fig. 1C, left panel). To directly observe these fusion events, we performed time-lapse imaging at 2-minute intervals. Fusion was defined as the merging of two foci that subsequently moved together during several successive images (Fig. 1D). Most fusion events occurred between 70 to 90 minutes post-induction, corresponding to ~75-90 % of chromosome degradation (dotted line). By T120, when chromosome degradation was completed, fusion events had occurred in 95% of the cells, as shown by the cumulative curve (black line).

To assess whether plasmid size affects condensates fusion, we repeated the experiment using a ~10-kbp mini-F plasmid (pJYB234). Similar coalescence kinetics were observed, with over 90 % of the cells exhibiting fusion events, as with the 100-kbp plasmid (Fig. 1C, central panel and Supplementary Fig. S1D). This finding indicate that condensate fusion is independent of plasmid size.

To ensure that plasmids do not spontaneously cluster together in the absence of the chromosome, we measured the behavior of a mini-F lacking the *par* system, labelled with a FROS system (Fig. 1C, right panel). Due to partitioning defect, this Δ*par* mini-F (pPER07) was frequently lost, resulting in a high proportion of plasmid-less cells, *i.e.* cells without foci (62%). Among cells retaining the plasmid, the proportion with one (17.3%) or two (16.9%) foci remained unchanged before (T0) and after complete chromosome degradation (T120). This result demonstrates that, in nucleoid-free cell, low-copy-number plasmids do not cluster together in the absence of ParABS.

Defects in ParB multimerization or ParA function similarly impair condensate fusion

To further investigate whether the fusion events observed in nucleoid-free cells are an intrinsic property of ParB condensates, we examined a ParB variant, $ParB_F$-R156A, which partially impairs condensate formation and partition activity (Delimi et al., 2025). This mutation, located in the box III motif involved in CTP binding and hydrolysis (Osorio-Valeriano et al., 2021) still allows $ParB_F$-R156A to bind to $parS_F$ and form clamps but disrupts ParB-ParB interactions necessary for larger condensate formation (Delimi et al., 2025). To test whether the assembly of $ParB_F$-R156A at $parS_F$ can coalesce, we imaged cells carrying an F plasmid expressing $ParB_F$-R156A-mVenus before (T0) and after I-SceI induction (Fig. 2A, top panel). At T0, 15% of the cells lacked foci due to plasmid loss, reflecting impaired partitioning due to the $parB_F$-R156A mutation (Fig. 2A, bottom panel), compared to 1.5 % in the wild-type (Fig. 1C). At T120, a shift from two foci to one was observed, indicating some degree of coalescence. However, the change was modest: the proportion of one-focus cells increased by ~18%, and two-focus cells decreased by ~19%, in contrast to 58% and 47%, respectively, for the WT. Moreover, at T120 only 50 % of chromosome-depleted cells exhibited fusion events with delayed kinetics (Fig. S1E), compared to ~95% in wild-type (Fig. 1D). These results indicate that partial defects in ParB condensate assembly substantially reduce the frequency and efficiency of foci fusion.

$ParA_F$ is known to play a critical role in positioning partition complexes along the nucleoid (Hu et al., 2021; Le Gall et al., 2016). In its ATP-bound form, $ParA_F$ interacts with both $ParB_F$ and non-specific DNA (nsDNA) (Bouet et al., 2007; Castaing et al., 2008). We therefore tested whether $ParA_F$ contributes to condensate fusion by analyzing a plasmid F Δ$parA_F$ (F1-10B12), in which $ParB_F$-mVenus is expressed from an inducible P*tet* promoter. Western blot analyses showed that $ParB_F$-mVenus production was about half that of the wild-type expressed from its native $ParA_F$ auto-regulated promoter (Fig. S2). Despite this reduction, partition condensates

were readily observed (Fig. 2B, top). We quantified the number of ParB foci per cell before (T0) and after (T120) I-SceI induction (Fig. 2B, bottom). At T0, 43% of the cells were plasmid-less, consistent with defective partitioning due to the Δ*parA*$_F$ mutation (Le Gall et al., 2016). At T120, only a slight shift was observed: the proportion of one-focus cells increased by 7%, while two-focus cells decreased by 6.4%. This contrasted sharply with the wild-type condition (Fig. 1D), indicating that ParA$_F$ plays a role in efficient coalescence of ParB condensates in the absence of chromosome.

In both *parB*$_F$-R156A and Δ*parA*$_F$ conditions, we noted a pronounced increase in diffuse ParB-mVenus fluorescence with less-defined condensates compared to the WT plasmid. To quantify this result, we performed skewness analysis, a metric reflecting the asymmetry of the intracellular distribution of fluorescence intensity. Higher skewness values correspond to a few bright pixels for a majority of low intensity pixels, or punctate foci (*i.e.*, well-formed condensates), while near zero skewness values indicate diffuse fluorescence. The skewness thus provides a quantitative proxy for estimating the ParB assembly of condensates (Fig. 2C). In WT plasmid, ParB condensates appear as bright foci leading to an average skewness of 1.85 (N=144). In contrast, in cells carrying a mini-F Δ*parS* plasmid (which cannot nucleate ParB condensates), skewness dropped to a baseline of 0.19 (N=411). The *parB*$_F$-R156A and Δ*parA*$_F$ conditions showed intermediate skewness values of 0.70 (N=269) and 0.72 (N=152), respectively, indicating partial defects in condensate formation. These defects likely stem from impaired interactions between ParB molecules following loading at *parS*$_F$, preventing the condensation of the majority of ParB (see discussion).

Together, these results shows that, in the absence of the nucleoid, coalescence events are severely impaired when ParB self-association is disrupted, which is accompanied by defects in condensate assembly. We conclude that both the assembly and the coalescence of ParB condensates are dependent on functional, activated ParB-ParB interactions.

Coalescence into a single condensate is a conservative process

Condensates naturally tend to fuse into fewer, larger assemblies, as droplet coalescence minimizes surface tension and free energy, thereby reaching a more thermodynamically stable state (Hyman et al., 2014). However, the diffraction limit of fluorescence microscopy prevented us from directly measuring the size of individual ParB condensates before and after fusion. To overcome this technical limitation, we used fluorescence intensity as a proxy for condensate size. This approach relies on our previous finding that the ParB concentration inside

condensates is comparable to the overall protein concentration in the cytoplasm, suggesting that condensates accumulate ParB up to a cytoplasmic saturation threshold (Guilhas et al., 2020). Under these conditions, fluorescence intensity is thus expected to scale with condensate volume.

We measured the fluorescence intensity of ParB-mVenus foci in 50 cells, before and after fusion events. On average, the post-fusion intensity was 0.94 times the sum of the two pre-fusion foci (Fig. 3A and Fig. S3). This indicates that the majority of ParB molecules are retained within the resulting condensate, consistent with a conservative coalescence process in which little to no ParB is lost or dispersed. This finding supports the idea that fusion results in the formation of larger condensates.

We next asked whether more than two foci can coalesce into a single one. To test this, we treated cells with cephalexin, a β-lactam antibiotic that blocks cell division without inhibiting DNA replication. This treatment led to cell elongation and increased the plasmid copy number per cell. After one hour of cephalexin treatment, cells approximately doubled in size, and ParB foci ranged from 1 to 8, with an average of 4.2 foci per cell (Fig. 3B). Following chromosome degradation, 88% of cells displayed a single ParB focus at T120, indicating that most ParB condensates had fused into a single one.

These findings support the view that ParB condensates behave as droplets undergoing coalescence. Regardless of plasmid copy number, ParB condensates reliably fuse into fewer, larger assemblies to minimize surface tension. This process is largely conservative, retaining all ParB molecules within the fused condensates.

ParB-DNA condensates operate near the fusion-separation boundary

Our measurements showed that 95 % of chromosome-depleted cells had undergone partition condensates fusion within 120 min of chromosome degradation induction (Fig. 1E). We were curious about the remaining ~5% of cells in which fusion was not observed at T120. Closer inspection revealed that some cells displaying a single fused focus at earlier time points latter exhibited splitting events. To explore this phenomenon, we performed high-frequency imaging, acquiring frames every 250 milliseconds over 30-second (Fig. 4A). Despite this brief time window, we detected splitting events in ~10 % of cells carrying the plasmid F (Fig. 4B), suggesting that splitting is a frequent event, potentially occurring approximately once every five minutes per cell on average. When examining cells carrying the smaller mini-F, splitting events were detected in 18% of cells, indicating that condensates derived from smaller plasmids split more frequently than those from larger plasmids. This suggests that, in the absence of

chromosome, a smaller DNA amount near *parS* sites permits more frequent escape of one plasmid from condensates. Moreover, the frequency of splitting events was slightly higher in Δ*parA* derivatives (Fig. 4B), suggesting that fused condensates formed either from smaller DNA molecules or in the absence of ParA are more prone to dissociation. In all cases, however, splitting events were transient, as the separated foci consistently fused back after a short period of time (Fig. 4A).

In nucleoid-depleted cells, condensates are fused ~90% of the time but still undergo occasional splitting, suggesting that the system operates near a crossover regime between fused and separated states, with a free energy difference approaching zero, *i.e.*, within the fused region of the phase diagram but close to the transition line ($\Delta F \sim 0$). To quantitatively understand this equilibrium, we developed a coarse-grained polymer model that captures the competition between surface energy minimization and configurational entropy loss during condensate coalescence (see Supplementary Methods). At the fusion-separation transition, we estimated a critical surface tension γ_{crit} = 0.80 +/- 0.21 µN.m^{-1} for the F plasmid (N = 660; Figure S6). Given that ParABS systems are naturally found on replicons spanning a wide range of size, from ~25 kbp to over 1 Mb (Planchenault et al., 2020), we extend our analysis and calculated a γ_{crit} = 1.10 +/- 0.29 µN.m^{-1} for a 1 Mb DNA molecule. For the smaller mini-F used in this study (pJYB234, ~10 kbp; N = 60), we measured a γ_{crit} = 0.49 +/- 0.13 µN.m^{-1} (Figure S6). These values place the tension surface of ParB-DNA droplets, across a large range of DNA size replicons, within the typical 0.1-1 µN.m^{-1} range observed in biological phase-separated systems (Holland et al., 2023). This supports the conclusion that ParB-DNA condensates operate near the fusion-separation boundary, with entropy costs remaining negligible over biologically relevant DNA lengths.

Coalescence of partition condensates occurs rapidly

The dynamic splitting-fusion behavior observed for ParB foci provided an opportunity to investigate the kinetics of condensate coalescence. Using the frame where a splitting event was first observed as time zero, we measured the time required for ParB condensates to fuse back together. Analysis of 111 such events from the F plasmid revealed that re-fusions occurred, on average, within approximately one second (Fig. 4C). This result demonstrates that coalescence of partition condensates is a rapid process, nearly instantaneous compared to the time of splitting, the cell cycle or to DNA replication. To further characterize the fusion kinetics, we plotted the number of fusion events over time on a log-log scale and found that the distribution

fit well to a power law with an exponent of -3/2 (Fig. 4C, inset). This scaling suggests that the coalescence times are consistent with a first encounter of two Brownian particles (Byczkowski et al., 2013). Such behavior is consistent with rapid, free diffusion of condensates in the absence of chromosome, where condensate collisions and subsequent fusions are governed by random Brownian motion.

To assess the mobility of partition condensates, we compared their diffusive behavior in the presence and absence of the chromosome. $ParB_F$-mVenus foci from both plasmid F and mini-F were tracked using high-resolution time-lapse microscopy, with images acquired every 0.5 second over a 30 second period. In chromosome-depleted cells, condensates exhibited markedly enhanced mobility (Fig. S4): the mean step size (*Ss*) between frames increased by 6-fold for mini-F (*Ss* ~ 1.8 µm) and 4-fold for plasmid F (*Ss* ~ 1.2 µm) compared to cells with intact chromosomes (*Ss* ~ 0.3 µm). We quantified this difference by computing the mean square displacement (MSD) of $ParB_F$ foci to estimate diffusion coefficients (*D*) under both conditions (Fig. 4D and Fig. S4), using a sub diffusive model:

$$MSD(t) = D_\alpha \, . \, t^{\alpha}$$

where D_α is the generalized diffusion coefficient (µm² $s^{-\alpha}$) and α is the scaling exponent describing the nature of particle motion (see Eq. (5) in Supplemental methods). In the presence of the chromosome, α values of 0.81 (F) and 0.88 (mini-F) reflected sub-diffusive, constrained dynamics (Parry et al., 2014). Upon chromosome removal, α rose to 0.92 and 0.95, respectively, approaching the theoretical value for Brownian (free) diffusion (α = 1). The corresponding D_α values increased by 10-40 fold, from 0.001-0.002 µm² $s^{-\alpha}$ to 0.04 and ~0.02 µm² $s^{-\alpha}$, indicating a major release of partition complexes from the $ParA_F$-nucleoid tethering (Hu et al., 2021; Le Gall et al., 2016). Notably, the rise in D_α scales approximately with the square of the step size, confirming that the exponents α are sufficiently close to 1 to approximate D_α to an usual diffusion coefficient at short time scales. Together, these results show that ParB condensates behave as nearly freely diffusing particles in the absence of chromosome, and suggest that their mobility is primarily limited by condensate size rather than the length of the plasmid DNA carrying $parS_F$.

Partition condensates assemble and disassemble within seconds

In biological phase separation, biomolecular interactions, such as protein-protein and protein-nucleic acid interactions, underpin the formation and stability of condensates. The ParB condensates formed on plasmid F enables the dissection of the individual roles of these two

interactions within cells almost completely depleted of non-specific DNA. To test the role of weak intermolecular interactions in condensate stability, we used 1,6-hexanediol (Hex), an aliphatic alcohol that interferes with hydrophobic interactions and has the ability to disrupt some liquid-like condensates, but not solid-like aggregates or protein-DNA complexes (Kroschwald, 2017).

Cells expressing $ParB_F$-mTq2 from mini-F along with a FROS reporter MalI-mNG[2] (bound to 7 *malO* sites present on the plasmid, pPER08) were deprived from their chromosome and, when ~95% of cells displayed fused partition condensates (T120), were treated with 10 % Hex. After one minute, ParB-mTq2 fluorescence became diffuse in most cells (89.3%), indicating efficient condensates dissolution (Fig. 5A and Fig. S5). In contrast, MalI-mNG2 foci remained intact, showing that specific protein-DNA interactions were preserved. Interestingly, some cells displayed two MalI foci following Hex treatment, suggesting that plasmids, previously held together within the same condensate, were now free to diffuse apart, further supporting that coalescence is mediated by weak and/or non-specific interactions (Fig. S5A).

To investigate the kinetics of ParB condensate disassembly, we performed time-lapse imaging during Hex infusion (Fig. 5B, top left). ParB fluorescence became visibly diffuse as early as 7 seconds after treatment and foci disappeared almost completely by 47 seconds. To quantify the Hex-induced disassembly, we measured the fluorescence skewness across 1150 cells (Fig. 5B, right). Before Hex addition, skewness was ~2.11, slightly higher than measured in the presence of nucleoid (1.85; Fig. 2C). Upon Hex treatment, the average skewness progressively decreased to ~0.84 and 0.47 after 7 and 27 seconds, respectively, reaching a plateau at ~0.33 by 47 seconds. This plateau value is slightly above the skewness observed when all ParB are diffusive (0.19; Fig. 2C), consistent with a small fraction of ParB remaining bound to *parS* or clamped nearby.

We then tested whether ParB condensates could reassemble after washing out Hex. Following a 100-seconds Hex exposure, cells were infused in buffer without Hex (Fig. 5B, bottom left). Within 7 seconds, skewness rapidly increased to 1.49, and by 27 seconds, it reached a value above 2, restoring the pre-treatment level and showing complete ParB condensates reassembly (Fig. 5B, right). Strikingly, the kinetics of reassembly mirrored that of disassembly, both occurring within seconds.

Altogether, these data demonstrate that ParB condensates disassemble and reassemble rapidly and reversibly in response to disruption and restoration of weak hydrophobic interactions, respectively. In the absence of the nucleoid, this behavior strongly suggests that

the internal cohesion of partition condensates is primarily driven by reversible ParB-ParB interactions.

Partition condensates assembly requires both ParB-ParB and ParB-DNA interactions

To assay the relative contributions of ParB-ParB and ParB-nsDNA interactions to condensate assembly, we repeated the hexanediol treatment experiments in cells with an intact nucleoid (Fig. 5C). Under this condition, condensate disassembly occurred as rapidly as in nucleoid-depleted cells, with skewness reaching a plateau within 47 seconds. Likewise, upon Hex washout, ParB condensates reassembled within 30 seconds, indicating that the disruption and restoration of ParB-ParB interactions proceed with comparable kinetics in the presence or absence of the nucleoid. However, while the disassembly was nearly complete in nucleoid-free cells (plateau skewness ~0.33), it was only partial in the presence of the chromosome, with skewness stabilizing around ~1.2. This suggests that, while ParB-ParB interactions are required for full condensate formation, ParB-DNA interactions, likely nonspecific binding to the nucleoid, also contribute substantially to condensate integrity.

To further probe these interactions, we repeated the Hex treatment in cells carrying a plasmid F encoding the ParB-R156A variant (F1-10B15), which exhibits impaired ParB-ParB interactions and reduced condensate formation (Fig. 2A, C). In nucleoid-depleted cells, ParB-R156A-mVenus skewness dropped rapidly from 1.04 to 0.29 within 7 seconds, reaching a plateau at ~0.21 (Fig. S5B). This value closely matched that of fully diffuse ParB in the absence of condensates (~0.19; Fig. 2C), indicating near-complete dissolution. In the presence of the nucleoid, skewness decreased from 0.81 to 0.36, plateauing at ~0.28 (Fig. S5C), slightly higher than in the nucleoid-free conditions but still indicative of near-total condensate disassembly.

Notably, in both WT and ParB-R156A backgrounds, condensate disassembly was slower and less complete in the presence of the nucleoid compared to its absence (Fig. 5B, C and Fig. S5B, C). Conversely, condensate reassembly after Hex washout occurred slightly faster when the nucleoid was present. These kinetic differences highlight the contribution of ParB–nucleoid interactions in both stabilizing condensates against disruption and promoting their rapid reformation. It is also possible that hexanediol affects ParA–ParB interactions; thus, in chromosome-containing cells, ParA-mediated tethering may further enhance condensate stability.

Finally, side-by-side comparison of WT and ParB-R156A condensates across all conditions using skewness quantification (Fig. 5D) clearly supports that (i) condensate formation occurs in both nucleoid-containing and -depleted cells (a-d), (ii) both Hex treatment and the ParB-

R156A variant causes partial defects in condensate formation (compare c and e to a), indicating that ParB-ParB interactions are necessary but not sufficient to assemble ParB condensates, and (iii) removal of both ParB-ParB interactions (via Hex treatment) and the nucleoid (f) leads to complete condensate disassembly, demonstrating that both interactions act synergistically to maintain condensate integrity.

Together, these findings establish that ParB condensate assembly is a cooperative process driven by both ParB-ParB and ParB-DNA interactions, with maximal cohesion and stability requiring their combined action.

Discussion

ParB condensates as a paradox of DNA segregation

In this study, we investigated the dynamics of ParB condensates involved in bacterial DNA partition, uncovering key kinetic and mechanistic features that define their behavior *in vivo*. Faithful segregation of low-copy-number genetic elements requires at least two partition complexes to remain physically separated on either side of the septum before cell division. This requirements presents a fundamental paradox: biomolecular condensates formed by phase separation inherently tend to coalesce into a single droplet to minimize surface tension and free energy (Azaldegui et al., 2021). ParABS-mediated partition systems offer a powerful model for understanding how cells reconcile this conflict. Growing evidence indicates that ParB assemblies exhibit droplet-like properties both *in vivo* (Guilhas et al., 2020) and *in vitro* (Babl et al., 2022), making them well-suited to address how phase-separated condensates can remain stable as multiple entities inside a single bacterial cell.

Chromosome removal reveals coalescence dynamics

Previous work showed that ParB condensates eventually merge *in vivo* following ParA depletion (Guilhas et al., 2020). Yet, because the degron-based approach induced continuous ParA overproduction followed by its gradual degradation, fusion events became detectable only after overnight growth, thereby preventing accurate analysis of coalescence kinetics. To overcome this limitation, we developed a chromosome degradation approach that eliminates ParA function by removing its DNA matrix. This system allowed us to probe the intrinsic behavior of ParB condensates in the absence of nucleoid tethering, thereby allowing their unrestricted diffusion in the cytoplasm.

Nearly all ParB condensates have coalesced within 120 minutes of chromosome removal (Fig. 1B–D and Fig. S1), independently of their initial number (Fig. 3B). The resulting ParB

condensates exhibited high mobility, with diffusion coefficients reaching ~0.02 and ~0.04 $\mu m^2 s^{-1}$ for F and mini-F plasmids, respectively, which is more than 10-fold higher than in nucleoid-containing cells (~0.002 and ~0.001 $\mu m^2 s^{-1}$) (Fig. 4D and Fig. S4). These values are comparable to diffusion rates reported for large nucleoprotein assemblies in *E. coli*, such as polysomes (~0.04 $\mu m^2 s^{-1}$), but remain slower than those of free ribosomal subunits (~0.2 $\mu m^2 s^{-1}$) (Bakshi et al., 2012; Sanamrad et al., 2014). In nucleoid-free cells, the scaling exponent α calculated from the MSD curves approaches values close to 1 consistent with near-free Brownian motion, whereas in the presence of the chromosome, sub-diffusive values of α (<0.9) indicate constrained mobility. These findings also strongly suggest that, in the absence of the nucleoid, the mobility of ParB condensates is primarily governed by the physical size of the droplets rather than the length of the $parS_F$-carrying plasmid.

Using transient splitting of ParB condensates as a reference point, we measured fusion times of ~1 second (Fig. 4A-C). Such immediate coalescence upon contact indicates a droplet fusion process rather than Ostwald ripening (Hyman et al., 2014). Moreover, the power-law distribution of coalescence times mirrors the behavior of two Brownian particles undergoing a first encounter, underscoring the stochastic nature of condensate collisions. Strikingly, our analysis shows that ParB condensates operate near the fusion-separation boundary (Fig. S6), implying that only minimal energy is required either to separate fused droplets or to split condensates generated by partition complex duplication during replication. Operating at this boundary is likely crucial for DNA segregation, as it ensures that condensates remain dynamic enough to avoid irreversible coalescence into a single droplet. This finely tuned balance highlights how condensate phase behavior is optimized *in vivo* and raises the possibility that ParA may actively facilitate condensate separation with only a minimal energetic input. In light of this finding, the role of ParA in driving the separation of duplicated partition complexes or other condensates such as carboxysome (Ah-Seng et al., 2013; Byrne et al., 2025) warrants further investigation.

ParA regulates both condensate positioning and assembly

Our results also reveal that proper condensate assembly is essential for efficient coalescence. Indeed, perturbing the ability of ParB to form condensates, while preserving its capacity to bind to *parS* and diffuse nearby, impaired coalescence. This was observed both with the ParB-R156A variant and in the absence of ParA (Fig. 2). These findings suggest that the same molecular interactions underpin condensate assembly and coalescence in nucleoid-free cell, consistent with the droplet-like nature of ParB condensates.

Strikingly, our data uncouple two distinct roles of ParA. In addition to the tethering of ParB condensates to the nucleoid, which restricts their diffusion and prevents coalescence, ParA also promotes a condensate-competent state of ParB *in vivo*, likely by enhancing ParB-ParB interactions as observed *in vitro* (Taylor et al., 2021). Moreover, in the absence of ParA, splitting events became slightly more frequent, especially for ParB condensates assembled on large plasmids (Fig. 4B), suggesting that ParA also contributes to inter-droplet cohesion in nucleoid-free conditions. Together, these results identify ParA as a dual regulator that both positions partition complexes and activates their intrinsic phase-separation behavior.

Biophysical properties of ParB condensates

To further probe the biophysical properties of ParB condensates, we used 1,6-hexanediol (Hex), a compound known to disrupt weak hydrophobic interactions in some biocondensates (Kroschwald, 2017). In chromosome-depleted cells, Hex treatment triggered rapid and near-complete disassembly of ParB condensates, with fluorescent foci disappearing within seconds (Fig. 5A-B). This disassembly was fully reversible, as condensates reformed within seconds after Hex removal, restoring the initial fluorescence skewness levels, consistent with the highly dynamic and exchangeable nature of biocondensates (Ladouceur et al., 2020). Notably, the timescale of ParB condensate reassembly parallels that of ParB reloading after replication fork passage over *parS* centromere sites (Walter et al., 2020), providing a mechanistic basis for the robust and continuous presence of ParB condensates throughout the bacterial cell cycle.

To date, only a single exception to the persistent presence of ParB condensates has been reported. In the predatory bacterium *Bdellovibrio bacteriovorus*, $ParB_{Bbac}$ condensates are absent during a defined developmental stage despite expression of $ParB_{Bba}$ (Kaljevic et al., 2023). The molecular mechanism underlying this stage-specific suppression of condensate formation remains unknown, but it correlates with the presence of short DNA segments adjacent to the two *parS* sites. This suggests that the initial binding step to $parS_{Bbac}$ may be inhibited by specific DNA context or structure, and possibly regulated through the action of a developmentally controlled factor to prevent ParB condensates assembly.

Mechanistic model of nucleation and stabilization

In nucleoid-containing cells, Hex treatment induced only partial disassembly of ParB condensates, with fluorescence skewness plateauing at ~1.2 versus ~0.33 in nucleoid-free cells (Fig. 5B-C). This indicates that interactions with chromosomal DNA, likely through non-specific binding, stabilize ParB condensates and buffer them against disruption. Supporting this

view, the ParB-R156A variant, deficient in ParB-ParB interactions, displayed near-complete dissolution in both chromosomal contexts (Fig. 5D, Fig. S5B–C), highlighting the primary role of ParB multimerization in condensate formation, with ParB-DNA interactions acting as an additional stabilizing layer. Interestingly, the basal skewness measured in the presence of Hex (0.33) remained higher than that in the absence of *parS* (~0.19; Fig. 2C), suggesting that a fraction of ParB dimers remains bound to *parS* or persists as clamps on *parS*-flanking DNA. These residual, potentially activated ParBs may facilitate the rapid and efficient reassembly of condensates once hydrophobic interactions are restored. Altogether, these findings support a model in which ParB condensates emerge from cooperative ParB-ParB and ParB-DNA interactions. ParB bound to $parS_F$ and converted into clamps on flanking DNA likely serves as a nucleation site for droplet formation. These clamped ParB species would function as activation seeds for the recruitment of diffusive ParB, enabling the rapid and reversible condensate dynamics we observed. This mechanistic model aligns well with recent proposals suggesting that clamped ParB species are activated intermediates promoting condensate formation (Delimi et al., 2025).

In summary, our findings establish ParB partition complexes as *bona fide* biocondensates: they undergo rapid, reversible fusion and fission, display high mobility when untethered, and depend on multivalent interactions for assembly. We further show that ParA acts not only as a spatial positioning factor but also as a key regulator of condensate coalescence. This dual role ensures that multiple partition complexes remain as distinct entities properly positioned within the same cell, thereby securing faithful segregation.

More broadly, our findings provide a biophysical framework for understanding bacterial DNA segregation as a process governed by regulated phase separation and ParA-type ATPase dynamics. Partition condensates exemplify how bacterial cells can harness the physics of phase separation to achieve robust and controlled spatial organization. This work reinforces the concept that phase separation is a conserved and versatile mechanism for the compartmentalization and spatial positioning of membrane-less organelles, spanning both prokaryotic and eukaryotic systems.

Experimental procedures

Bacterial strains, plasmids and oligonucleotides

All strains used in this study are derivatives of *E. coli* K12 and are listed, together with plasmids, in Table S1. Details of plasmid and strain construction are provided in the Supplemental experimental procedures. Briefly, strain LY643, which harbors four I-SceI sites (gift from C.

Lesterlin), was modified to allow uniform induction of *para*$_{BAD}$*::I-sceI* by introducing the *Pcp18::araE* alleles (Bouet et al., 2006) via P1 transduction. To enhance chromosome DNA degradation efficiency, a *recA* mutation was also introduced, resulting in strain DLT4151.

All F and mini-F plasmids are derivatives of F1-10B (Debaugny et al., 2018) and pDAG114 (Bouet et al., 2006), respectively. F1-10B derivatives were introduced into recipient strains by conjugation, while pDAG114 derivatives were introduced by $CaCl_2$-transformation.

Epifluorescence microscopy

Strains expressing fluorescently tagged proteins were grown overnight at 30°C in M9 minimal medium supplemented with glucose and casamino acids (M9-glucose-CSA). Cultures were diluted 1:250 in fresh medium and incubated at 30°C until OD_{600nm} ~0.3. Cells were then either spotted (0.7 µl) onto M9-buffered 1% agarose pads or loaded into microfluidic devices (Chitozen slides, Idylle).

Fluorescence images were acquired as previously described (Diaz et al., 2015) using a Nikon epifluorescence microscope and NIS-Elements AR software (Nikon) for image capture and processing. Image analysis was performed using ImageJ softwares, with foci detection and positioning on the longitudinal cell axis carried out using the "*Coli inspector*" macro and the "*ObjectJ*" plugin, respectively.

For nucleoid staining, cells were incubated with DAPI (1 $\mu g.ml^{-1}$) for 10 min under shaking prior to loading into microfluidic slides, followed by continuous flow with M9-glucose medium containing DAPI (1 $\mu g.ml^{-1}$).

To quantify the ratio of ParB fluorescence intensity before and after fusion events, cells carrying two visible ParB condensates were selected. Regions of interest (ROIs) were manually drawn around each condensate in three consecutive frames before fusion, and the total fluorescence intensity was averaged. After fusion, a single ROI was drawn around the merged condensate and the fluorescence was averaged over three consecutive frames. Background fluorescence from the medium was subtracted from all intensity measurements.

Skewness analyses

Skewness measurements were calculated using MicrobeJ plugin "*skewness*". This parameter measures the asymmetry of the pixel intensity distribution relative to the average fluorescence within each cell, providing a quantitative readout of condensate presence and compactness.

Mean square displacement

Exponential growing cells, induced or not with 0.2% arabinose, were spotted onto 1% agarose pads buffered with M9-glucose medium. Time-lapse fluorescence microscopy was performed with images every 500 milliseconds over a 30-second period. ParB-mVenus foci were detected and tracked using the *TrackMate* plugin (Ershov et al., 2022) in Fiji. For each track, the position of the foci was recorded over time, and the MSD was calculated as a function of time lag. The diffusion coefficient (D) was estimated from the slope of the initial linear portion of the MSD curve, assuming Brownian diffusion. All fitting and statistical analyses were performed using custom scripts (See supplemental Material and methods for details).

Physical modeling

Details of the theoretical physics employed for physical modeling are described in Supplementary materials. It includes the description of polymer model and coarse-graining analyses, the calculation of the Critical surface tension (γ_{crit}) and of the free-energy equilibrium.

ACKNOWLEDGEMENTS

We are grateful to Julien Cayron and Christian Lesterlin for sharing the strain LY463 prior to publication. We are grateful to Jian Liu and Manuel Campos for critical reading of the manuscript and suggestions, and we thank Manuel Campos, Christian Lesterlin and Fabian Erdel for insightful discussions. We also thank all members of the GeDy (CBI) and the SCPN (L2C) teams for fruitful discussions. This work was supported by the CNRS 80Prime MITI grant (ANCODS) and by the Agence National pour la Recherche (ANR-24-CE12-1319).

AUTHOR CONTRIBUTIONS

Conceptualization, J.-Y.B.;

Data curation, P.R., J.-Y.B.;

Formal analysis, L.D., J.C., J.-Y.B., and J.-C.W.;

Funding Acquisition, J.-Y.B.;

Investigation, P.R., L.D., J.C., J.R., J.-C.W., and J.-Y.B.;

Methodology, P.R., L.D., J.R., J.-C.W., and J.-Y.B.;

Project administration, J.-Y.B.;

Resources, F.C., J.-C.W., J.-Y.B.;

Supervision, J.-C.W., J.-Y.B.;

Validation, P.R., L.D., J.-C.W., and J.-Y.B.;

Visualization, P.R., J.-C.W. and J.-Y.B.;

Writing – Original draft, P.R., L.D., F.C., J.-C.W. and J.-Y.B.;

Writing – Review & Editing, P.R., L.D., F.C., J.-C.W., and J.-Y.B.

CONFLICT OF INTEREST STATEMENT

The authors declare that they have no conflicts of interest with the contents of this article.

ETHICS STATEMENT

This article does not contain any studies with human or animal subjects.

REFERENCES

Ah-Seng, Y., Lopez, F., Pasta, F., Lane, D., and Bouet, J.Y. (2009). Dual role of DNA in regulating ATP hydrolysis by the SopA partition protein. J Biol Chem *284*, 30067-30075.

Ah-Seng, Y., Rech, J., Lane, D., and Bouet, J.Y. (2013). Defining the role of ATP hydrolysis in mitotic segregation of bacterial plasmids. PLoS genetics *9*, e1003956.

Al-Husini, N., Tomares, D.T., Bitar, O., Childers, W.S., and Schrader, J.M. (2018). alpha-Proteobacterial RNA Degradosomes Assemble Liquid-Liquid Phase-Separated RNP Bodies. Mol Cell *71*, 1027-1039 e1014.

Alaoui, H.S., Quebre, V., Delimi, L., Rech, J., Debaugny-Diaz, R., Labourdette, D., Campos, M., Cornet, F., Walter, J.C., and Bouet, J.Y. (2025). In vivo assembly of bacterial partition condensates on circular supercoiled and linear DNA. Mol Microbiol *123*, 232-244.

Alberti, S., Arosio, P., Best, R.B., Boeynaems, S., Cai, D., Collepardo-Guevara, R., Dignon, G.L., Dimova, R., Elbaum-Garfinkle, S., Fawzi, N.L., *et al.* (2025). Current practices in the study of biomolecular condensates: a community comment. Nature communications *16*, 7730.

Azaldegui, C.A., Vecchiarelli, A.G., and Biteen, J.S. (2021). The emergence of phase separation as an organizing principle in bacteria. Biophys J *120*, 1123-1138.

Babl, L., Giacomelli, G., Ramm, B., Gelmroth, A.K., Bramkamp, M., and Schwille, P. (2022). CTP-controlled liquid-liquid phase separation of ParB. J Mol Biol *434*, 167401.

Bakshi, S., Siryaporn, A., Goulian, M., and Weisshaar, J.C. (2012). Superresolution imaging of ribosomes and RNA polymerase in live Escherichia coli cells. Mol Microbiol.

Basalla, J.L., Mak, C.A., Byrne, J.A., Ghalmi, M., Hoang, Y., and Vecchiarelli, A.G. (2023). Dissecting the phase separation and oligomerization activities of the carboxysome positioning protein McdB. eLife *12*.

Boeynaems, S., Alberti, S., Fawzi, N.L., Mittag, T., Polymenidou, M., Rousseau, F., Schymkowitz, J., Shorter, J., Wolozin, B., Van Den Bosch, L., *et al.* (2018). Protein Phase Separation: A New Phase in Cell Biology. Trends Cell Biol *28*, 420-435.

Bouet, J.Y., Ah-Seng, Y., Benmeradi, N., and Lane, D. (2007). Polymerization of SopA partition ATPase: regulation by DNA binding and SopB. Mol Microbiol *63*, 468-481.

Bouet, J.Y., Bouvier, M., and Lane, D. (2006). Concerted action of plasmid maintenance functions: partition complexes create a requirement for dimer resolution. Mol Microbiol *62*, 1447-1459.

Bouet, J.Y., and Funnell, B.E. (2019). Plasmid Localization and Partition in Enterobacteriaceae. EcoSal Plus *8:10.1128/ecosalplus.ESP-0003-2019*.

Byczkowski, T., Małecki, J., and Ryznar, M. (2013). Hitting times of Bessel processes. Potential Analysis *38*, 753-786.

Byrne, J.A., Swasthi, H.M., Hu, L., Azaldegui, C.A., Liu, J., and Vecchiarelli, A.G. (2025). Tuning the interaction of a ParA-type ATPase with its partner separates bacterial organelle positioning from partitioning. bioRxiv *2025.05.22.655647*.

Castaing, J.P., Bouet, J.Y., and Lane, D. (2008). F plasmid partition depends on interaction of SopA with non-specific DNA. Mol Microbiol *70*, 1000-1011.

Cohan, M.C., and Pappu, R.V. (2020). Making the Case for Disordered Proteins and Biomolecular Condensates in Bacteria. Trends in biochemical sciences *45*, 668-680.

Debaugny, R.E., Sanchez, A., Rech, J., Labourdette, D., Dorignac, J., Geniet, F., Palmeri, J., Parmeggiani, A., Boudsocq, F., Anton Leberre, V., *et al.* (2018). A conserved mechanism drives partition complex assembly on bacterial chromosomes and plasmids. Mol Syst Biol *14*, e8516.

Delimi, L., Revoil, P., Bouet, J.-Y., and Walter, J.-C. (2025). The ParB-CTP cycle activates phase separation in bacterial DNA segregation Nucleic Acids Res *53*, gkaf944.

Diaz, R., Rech, J., and Bouet, J.Y. (2015). Imaging centromere-based incompatibilities: Insights into the mechanism of incompatibility mediated by low-copy number plasmids. Plasmid *80*, 54-62.

Ershov, D., Phan, M.S., Pylvanainen, J.W., Rigaud, S.U., Le Blanc, L., Charles-Orszag, A., Conway, J.R.W., Laine, R.F., Roy, N.H., Bonazzi, D., *et al.* (2022). TrackMate 7: integrating state-of-the-art segmentation algorithms into tracking pipelines. Nat Methods *19*, 829-832.

Guilhas, B., Walter, J.C., Rech, J., David, G., Walliser, N.O., Palmeri, J., Mathieu-Demaziere, C., Parmeggiani, A., Bouet, J.Y., Le Gall, A., *et al.* (2020). ATP-Driven Separation of Liquid Phase Condensates in Bacteria. Mol Cell *79*, 293-303 e294.

Holland, J., Castrejon-Pita, A.A., Tuinier, R., Aarts, D., and Nott, T.J. (2023). Surface tension measurement and calculation of model biomolecular condensates. Soft matter *19*, 8706-8716.

Hu, L., Rech, J., Bouet, J.Y., and Liu, J. (2021). Spatial control over near-critical-point operation ensures fidelity of ParABS-mediated DNA partition. Biophys J *120*, 3911-3924.

Hu, L., Vecchiarelli, A.G., Mizuuchi, K., Neuman, K.C., and Liu, J. (2015). Directed and persistent movement arises from mechanochemistry of the ParA/ParB system. Proc Natl Acad Sci U S A *112*, E7055-7064.

Hwang, L.C., Vecchiarelli, A.G., Han, Y.W., Mizuuchi, M., Harada, Y., Funnell, B.E., and Mizuuchi, K. (2013). ParA-mediated plasmid partition driven by protein pattern self-organization. Embo J *32*, 1238-1249.

Hyman, A.A., Weber, C.A., and Julicher, F. (2014). Liquid-liquid phase separation in biology. Annual review of cell and developmental biology *30*, 39-58.

Kaljevic, J., Tesseur, C., Le, T.B.K., and Laloux, G. (2023). Cell cycle-dependent organization of a bacterial centromere through multi-layered regulation of the ParABS system. PLoS genetics *19*, e1010951.

Kroschwald, S., Maharana, S, Simon, A. (2017). Hexanediol: a chemical probe to investigate the material properties of membrane-less compartments. Matters *3*, e201702000010.

Ladouceur, A.M., Parmar, B.S., Biedzinski, S., Wall, J., Tope, S.G., Cohn, D., Kim, A., Soubry, N., Reyes-Lamothe, R., and Weber, S.C. (2020). Clusters of bacterial RNA polymerase are biomolecular condensates that assemble through liquid-liquid phase separation. Proc Natl Acad Sci U S A *117*, 18540-18549.

Le Gall, A., Cattoni, D.I., Guilhas, B., Mathieu-Demaziere, C., Oudjedi, L., Fiche, J.B., Rech, J., Abrahamsson, S., Murray, H., Bouet, J.Y., *et al.* (2016). Bacterial partition complexes segregate within the volume of the nucleoid. Nature communications *7*, 12107.

Lin, D.C.H., and Grossman, A.D. (1998). Identification and characterization of a bacterial chromosome partitioning site. Cell *92*, 675-685.

Livny, J., Yamaichi, Y., and Waldor, M.K. (2007). Distribution of centromere-like parS sites in bacteria: insights from comparative genomics. J Bacteriol *189*, 8693-8703.

Lutkenhaus, J. (2012). The ParA/MinD family puts things in their place. Trends in microbiology.

MacCready, J.S., Basalla, J.L., and Vecchiarelli, A.G. (2020). Origin and Evolution of Carboxysome Positioning Systems in Cyanobacteria. Mol Biol Evol.

MacCready, J.S., Hakim, P., Young, E.J., Hu, L., Liu, J., Osteryoung, K.W., Vecchiarelli, A.G., and Ducat, D.C. (2018). Protein gradients on the nucleoid position the carbon-fixing organelles of cyanobacteria. eLife *7*.

Monterroso, B., Margolin, W., Boersma, A.J., Rivas, G., Poolman, B., and Zorrilla, S. (2024). Macromolecular Crowding, Phase Separation, and Homeostasis in the Orchestration of Bacterial Cellular Functions. Chemical reviews *124*, 1899-1949.

Osorio-Valeriano, M., Altegoer, F., Das, C.K., Steinchen, W., Panis, G., Connolley, L., Giacomelli, G., Feddersen, H., Corrales-Guerrero, L., Giammarinaro, P.I., *et al.* (2021). The CTPase activity of ParB determines the size and dynamics of prokaryotic DNA partition complexes. Mol Cell *81*, 3992-4007 e3910.

Osorio-Valeriano, M., Altegoer, F., Steinchen, W., Urban, S., Liu, Y., Bange, G., and Thanbichler, M. (2019). ParB-type DNA Segregation Proteins Are CTP-Dependent Molecular Switches. Cell *179*, 1512-1524 e1515.

Parry, B.R., Surovtsev, I.V., Cabeen, M.T., O'Hern, C.S., Dufresne, E.R., and Jacobs-Wagner, C. (2014). The bacterial cytoplasm has glass-like properties and is fluidized by metabolic activity. Cell *156*, 183-194.

Pillet, F., Sanchez, A., Lane, D., Anton Leberre, V., and Bouet, J.Y. (2011). Centromere binding specificity in assembly of the F plasmid partition complex. Nucleic Acids Res *39*, 7477-7486.

Planchenault, C., Pons, M.C., Schiavon, C., Siguier, P., Rech, J., Guynet, C., Dauverd-Girault, J., Cury, J., Rocha, E.P.C., Junier, I., *et al.* (2020). Intracellular Positioning Systems Limit the Entropic Eviction of Secondary Replicons Toward the Nucleoid Edges in Bacterial Cells. J Mol Biol *432*, 745-761.

Sanamrad, A., Persson, F., Lundius, E.G., Fange, D., Gynna, A.H., and Elf, J. (2014). Single-particle tracking reveals that free ribosomal subunits are not excluded from the Escherichia coli nucleoid. Proc Natl Acad Sci U S A *111*, 11413-11418.

Sanchez, A., Cattoni, D.I., Walter, J.C., Rech, J., Parmeggiani, A., Nollmann, M., and Bouet, J.Y. (2015). Stochastic Self-Assembly of ParB Proteins Builds the Bacterial DNA Segregation Apparatus. Cell Syst *1*, 163-173.

Shin, Y., and Brangwynne, C.P. (2017). Liquid phase condensation in cell physiology and disease. Science *357*.

Soh, Y.M., Davidson, I.F., Zamuner, S., Basquin, J., Bock, F.P., Taschner, M., Veening, J.W., De Los Rios, P., Peters, J.M., and Gruber, S. (2019). Self-organization of parS centromeres by the ParB CTP hydrolase. Science *366*, 1129-1133.

Stracy, M., Schweizer, J., Sherratt, D.J., Kapanidis, A.N., Uphoff, S., and Lesterlin, C. (2021). Transient non-specific DNA binding dominates the target search of bacterial DNA-binding proteins. Mol Cell *81*, 1499-1514.

Taylor, J.A., Seol, Y., Budhathoki, J., Neuman, K.C., and Mizuuchi, K. (2021). CTP and parS coordinate ParB partition complex dynamics and ParA-ATPase activation for ParABS-mediated DNA partitioning. eLife *10*.

Vecchiarelli, A.G., Han, Y.W., Tan, X., Mizuuchi, M., Ghirlando, R., Biertumpfel, C., Funnell, B.E., and Mizuuchi, K. (2010). ATP control of dynamic P1 ParA-DNA interactions: a key role for the nucleoid in plasmid partition. Mol Microbiol *78*, 78-91.

Walter, J.C., Dorignac, J., Lorman, V., Rech, J., Bouet, J.Y., Nollmann, M., Palmeri, J., Parmeggiani, A., and Geniet, F. (2017). Surfing on Protein Waves: Proteophoresis as a Mechanism for Bacterial Genome Partitioning. Phys Rev Lett *119*, 028101.

Walter, J.C., Rech, J., Walliser, N.O., Dorignac, J., Geniet, F., Palmeri, J., Parmeggiani, A., and Bouet, J.Y. (2020). Physical Modeling of a Sliding Clamp Mechanism for the Spreading of ParB at Short Genomic Distance from Bacterial Centromere Sites. iScience *23*, 101861.

FIGURES LEGEND

Figure 1: ParB partition condensates coalescence in the absence of nucleoid.

A- Schematic representation of the inducible chromosome degradation system. I-Sce1 endonuclease cuts at the four specific sites. RecBCD complexes specifically degrade the chromosome but not plasmid DNA from the double strands breaks (black arrows).

B- Fluorescence microcopy of chromosome degradation and fusion events. Series of images of the same cell, stained with DAPI, at 40, 80 and 120 min post-arabinose induction, observed in the blue (left panels) and yellow (right panels) channels, to monitor chromosome degradation and ParB-mVenus condensates. Scale bar, 1 µm.

C- Distribution of the number of ParB-mVenus foci. The number of foci per cell before (T0; black) and after (T120; grey) chromosome degradation is displayed for the plasmid F (F1-10B04; left), the miniF (pJYB234; middle) and the miniF Δ*parAB* (pPER07; right).

D- Distribution of ParB-mVenus fusion events over time. Images (as in B) were acquired every two minutes between 40 and 120 min after arabinose induction. The number of cells displaying a fusion event were shown per time intervals. The solid line represents the cumulative fraction of chromosome-less cells displaying a fusion event. The dotted line represents the degradation of the chromosome over time (from Fig. S1B). N corresponds to the number of cell analyzed.

Figure 2: Coalescence depends on properly assembled ParB condensates

A- Time-lapse imaging of $ParB_F$-R156A-mVenus. (top) Series of images acquired at 0, 40, 80 and 120 minutes post-arabinose induction (plasmid F1-10B15). Scale bar, 1 µm. (bottom) Distribution of the number of ParB-R156A-mVenus foci before (T0; black) and after (T120; grey) chromosome degradation.

B- Time-lapse imaging of $ParB_F$-mVenus from the F Δ*parA* plasmid. As in (A), with the plasmid F1-10B12.

C- Quantification of the ParB condensates assembly defect. Fluorescent images of $ParB_F$-mVenus or $ParB_F$-R156A-mVenus, from WT (N=144), Δ*parA* (N=152), Δ*parS* (N=411) or *parB*-R156A (N=269) plasmids in exponentially growing cells (no chromosome degradation) were subjected to Skewness analyses. Skewness analyses were displayed as box plots indicating the medians, the quartiles and the standard deviations, and average values are indicated on top of each box plot.

Figure 3: Coalescence into a single condensate is conservative.

A- Most ParB molecules regroups in the fused condensates. The box plot displays the ratio of the average ParB fluorescence intensity, measured on three successive images, after fusion events over the average sum of ParB-mVenus fluorescence intensity from two foci, measured on three successive images, before fusion events. The box plots indicates the median, quartiles and the standard deviation, with each dot representing a fusion event (N=50).

B- Numerous ParB condensates coalesce into a single one after chromosome degradation.

(top) Imaging of $ParB_F$-mVenus from strain DLT 4161 (pJYB234), grown in the presence of cephalexin, after 40 and 120 min post-arabinose induction. The scale bar represents 1 µm. (bottom) Distribution of the number of ParB-mVenus foci before and after chromosome degradation. The number of foci per cell before (T0; black) and after (T120; grey) chromosome degradation is displayed for the plasmid mF pJYB234.

Figure 4: Coalescence of partition condensates is nearly instantaneous.

A- Transient splitting of ParB condensates in chromosome-depleted cells. Time-lapse fluorescence microscopy was performed after complete chromosome degradation (time > T120), with images acquired every 250 ms. Time is indicated in msec. Transient splitting and re-fusion of ParB-mVenus foci were frequently observed.

B- Splitting events are frequent. The frequency of splitting events was quantified in chromosome-depleted cells expressing ParB-mVenus from plasmid F or mini-F (mF), in the presence or absence of *parA* (Δ*parA*). N= 807 (F), 283 (mF), 120 (FΔ*parA*) and 86 (mFΔ*parA*).

C- Fusion occurs rapidly following splitting. A total of 111 chromosome-depleted cells carrying plasmid F and exhibiting a splitting event (as in A) were analyzed. The time elapsed between splitting and fusion was measured, revealing that fusion typically occurred within ~1 second. (*inset*) same data plotted in Log-Log scale (blue dots). The dotted red line corresponds to a power law with an exponent -3/2.

D- Partition condensates are highly mobile in the absence of the chromosome. Representative intracellular trajectories of ParB-mVenus foci tracked over time in cells carrying plasmid F or mini-F, either with (+chr) or without (no chr) the chromosome. Trajectories illustrate an important increase in mobility under chromosome-depleted conditions.

Figure 5: Assembly and disassembly of partition condensates occurs within seconds

A- Hexanediol disrupts ParB condensates but not DNA-bound proteins. Chromosome-depleted cells carrying the mini-F pJYB234 were imaged before (-Hex; left panels) and after (+Hex;

right panels) a 1-minute incubation with 10% 1,6-hexanediol in the blue (top panels) or yellow channels (bottom panels) to visualize $ParB_F$-mTq2 or MalI-mNG[2], respectively.

B- Rapid and reversible disassembly of ParB condensates in nucleoid-free cells. (left) Time-lapse imaging of chromosome-depleted cells expressing $ParB_F$-mVenus from plasmid F was performed using a microfluidic setup, allowing controlled infusion of hexanediol at time 0 (T0) and wash out at 100 sec (T100). (right) Quantification of $ParB_F$-mVenus fluorescence skewness across > 1700 cells at each indicated time point. The rapid decrease in skewness upon Hex treatment and the fast recovery upon washout indicates a nearly instantaneous disassembly and reassembly of ParB condensates.

C- Rapid, reversible but partial disassembly of ParB condensates in cells with an intact chromosome. Same as in (B) but performed in cells with a nucleoid. Hex was washed out after 160 s of infusion. Fluorescence skewness was calculated from > 760 cells per time point.

D- Multiple interactions are involved in ParB condensate assembly. Fluorescence skewness was measured in cells expressing either $ParB_F$ (WT) or the interaction-defective variant $ParB_F$-R156A, from plasmid F, imaged before (T0) or after (T120) chromosome degradation, and either untreated (–Hex) or treated (+Hex) with hexanediol. Time-lapse microscopy was performed as in (B–C). The skewness levels in f, g and h are 0.33, 0.27 and 0.21, respectively.

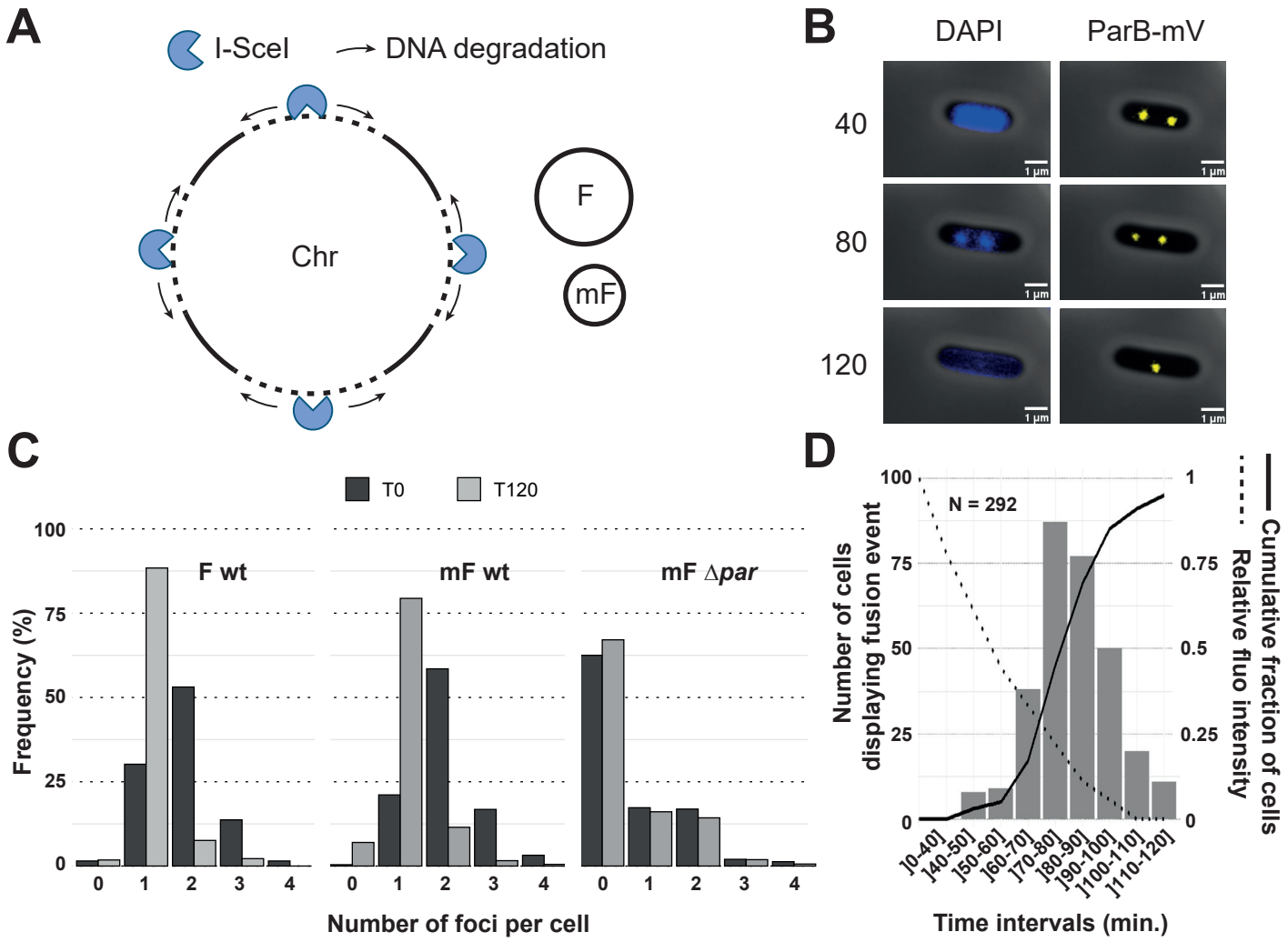
A
I-SceI
DNA degradation
Chr
F
mF
B
DAPI
ParB-mV
40
80
120
1 µm
C
T0
T120
F wt
mF wt
mF Δpar
Frequency (%)
Number of foci per cell
D
N = 292
Number of cells displaying fusion event
Cumulative fraction of cells
Relative fluo intensity
Time intervals (min.)
]0-40]
]40-50]
]50-60]
]60-70]
]70-80]
]80-90]
]90-100]
]100-110]
]110-120]

Figure 1

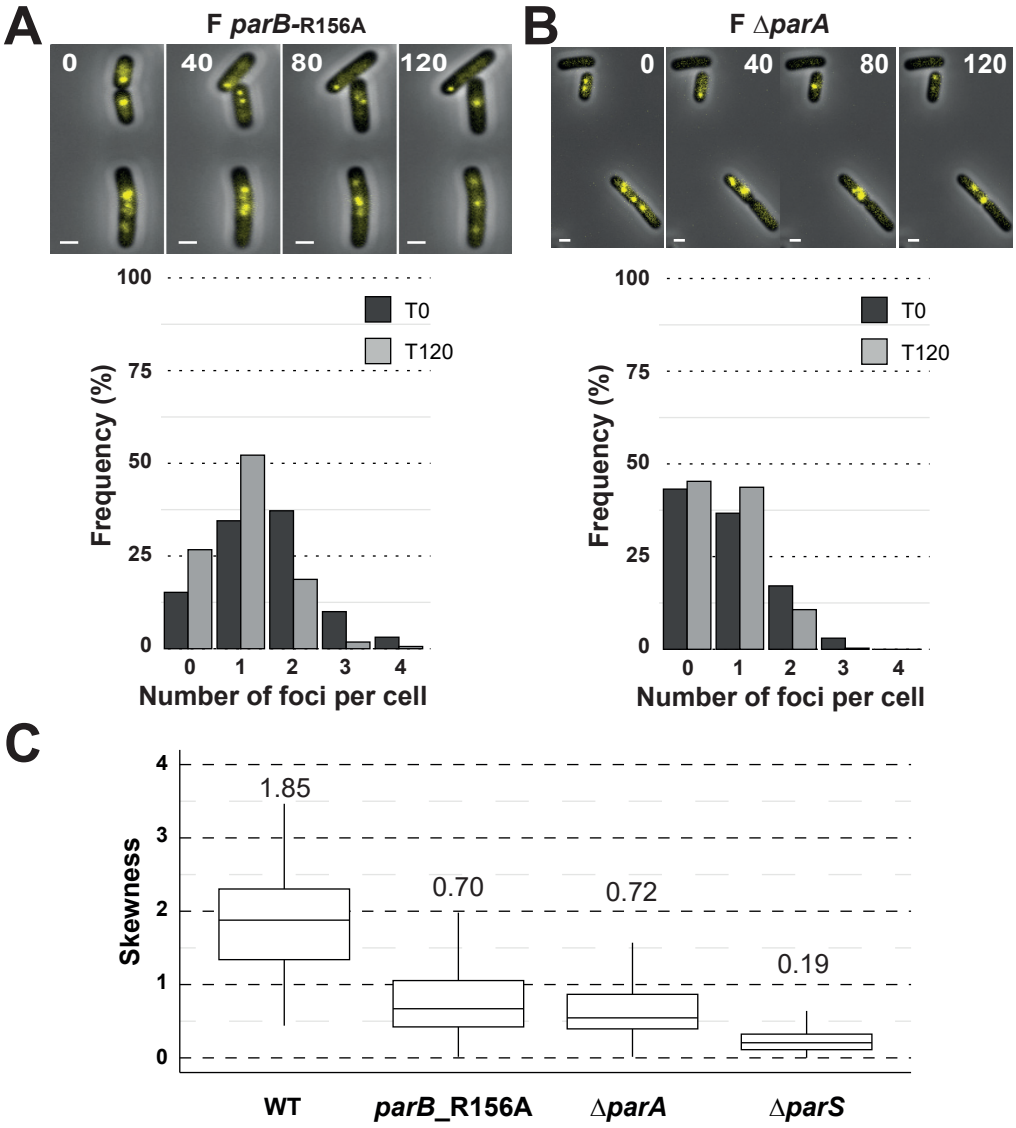
A
F parB-R156A
0
40
80
120
B
F ΔparA
0
40
80
120
100
75
50
25
0
Frequency (%)
T0
T120
0
1
2
3
4
Number of foci per cell
C
4
3
2
1
0
Skewness
1.85
0.70
0.72
0.19
WT
parB_R156A
ΔparA
ΔparS

Figure 2

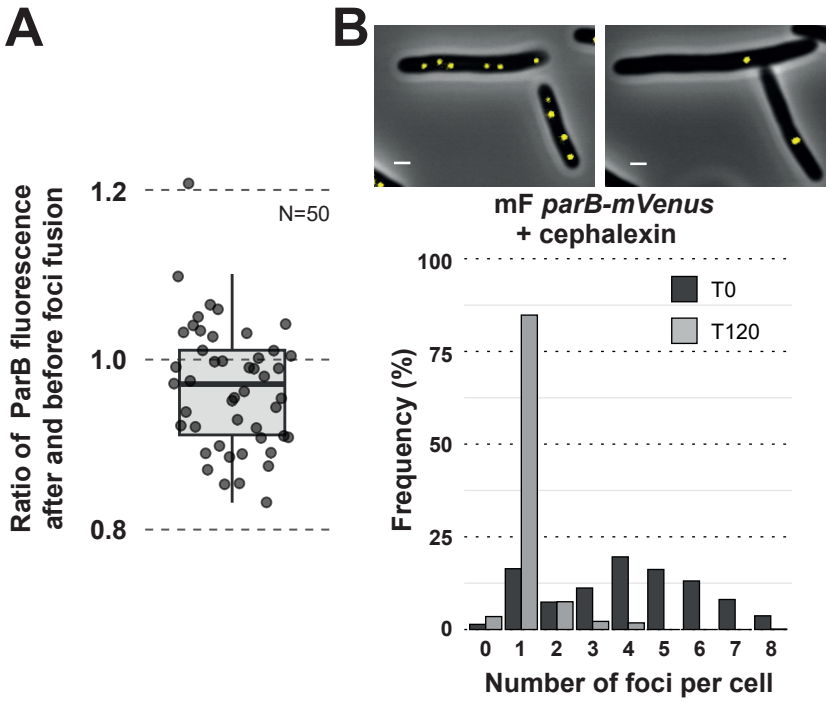
A
B
Ratio of ParB fluorescence after and before foci fusion
1.2
1.0
0.8
N=50
mF parB-mVenus
+ cephalexin
T0
T120
Frequency (%)
100
75
50
25
0
0 1 2 3 4 5 6 7 8
Number of foci per cell

Figure 3

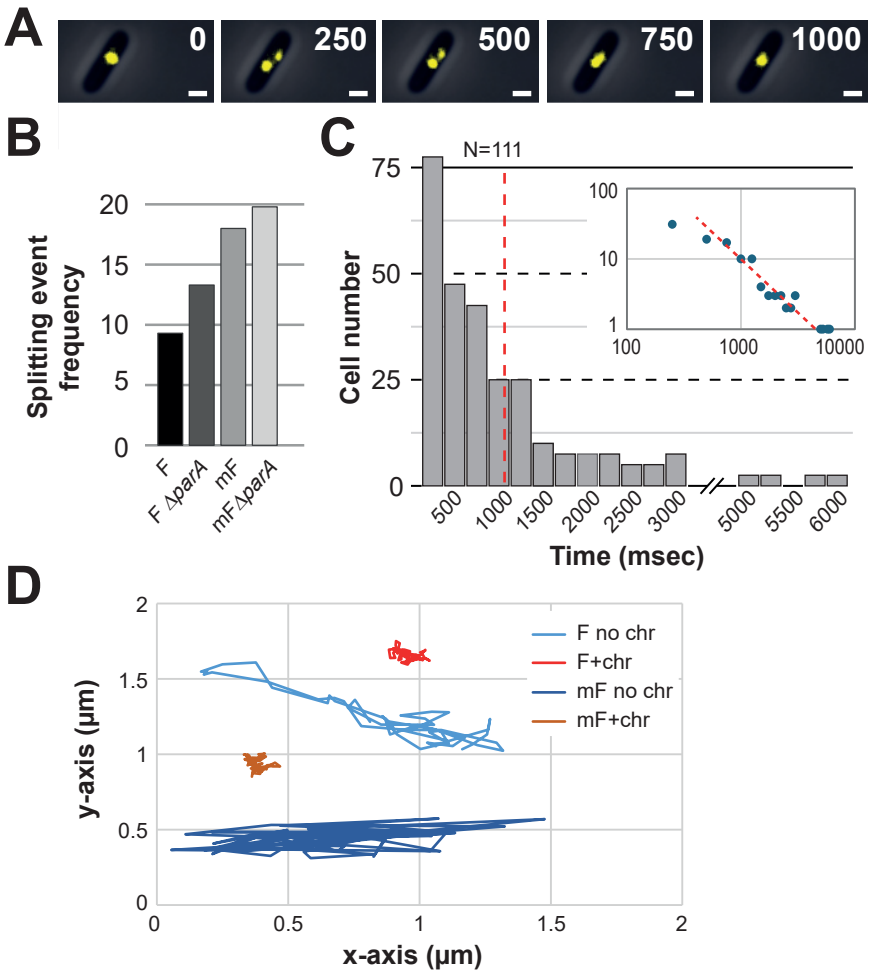
A
0
250
500
750
1000
B
Splitting event frequency
20
15
10
5
0
F
F ΔparA
mF
mF ΔparA
C
N=111
Cell number
75
50
25
0
100
10
1
100
1000
10000
500
1000
1500
2000
2500
3000
5000
5500
6000
Time (msec)
D
y-axis (µm)
2
1.5
1
0.5
0
0
0.5
1
1.5
2
x-axis (µm)
F no chr
F+chr
mF no chr
mF+chr

Figure 4

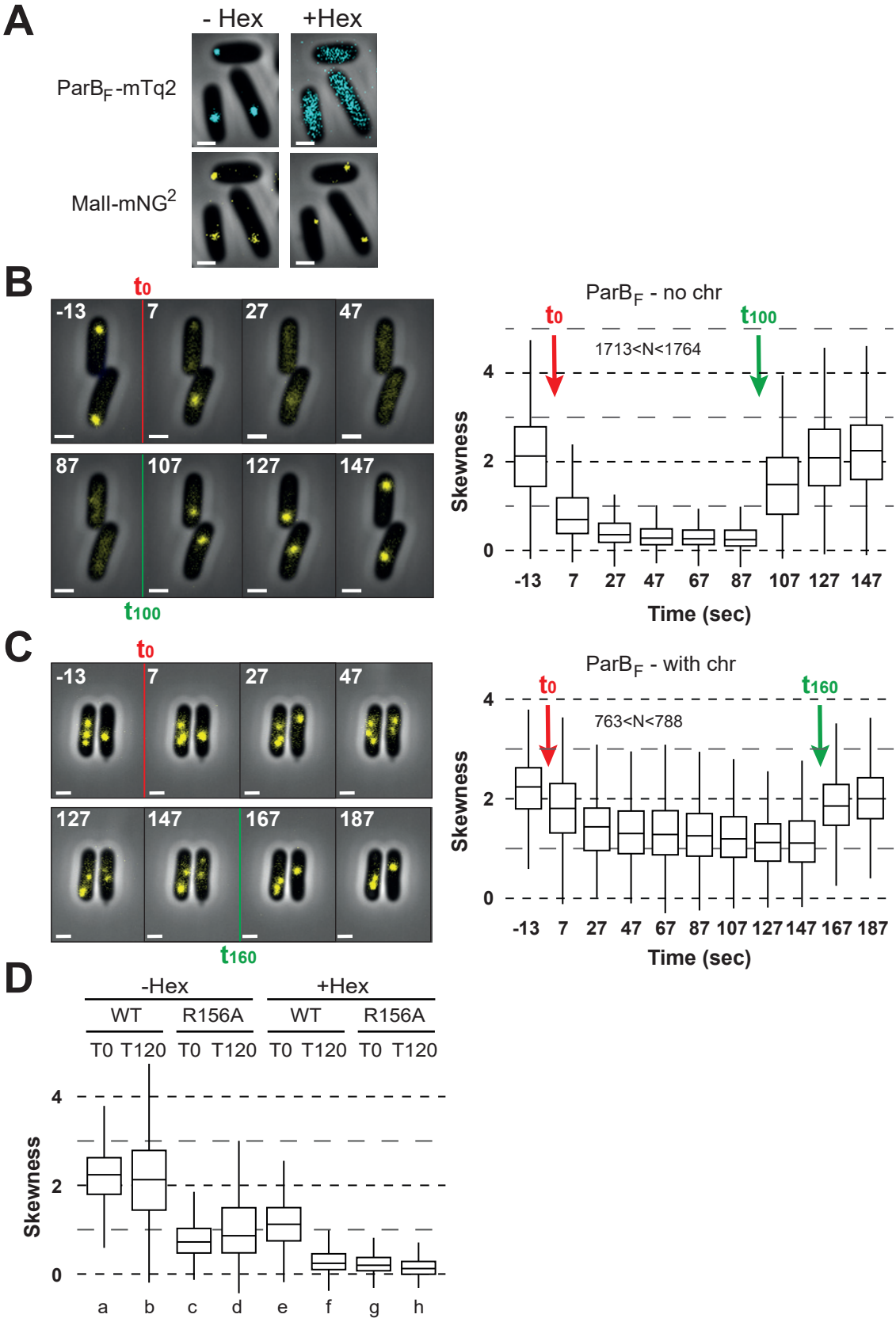
A
- Hex
+Hex
ParB$_F$-mTq2
MalI-mNG^2
B
t_0
-13
7
27
47
87
107
127
147
t_{100}
ParB$_F$ - no chr
1713<N<1764
Skewness
Time (sec)
C
t_0
127
147
167
187
t_{160}
ParB$_F$ - with chr
763<N<788
D
-Hex
+Hex
WT
R156A
T0 T120
a b c d e f g h

Figure 5